

Molecular dynamics simulation of ion dynamics within electrolyte of PEM Fuel Cells

S.S. Awulachew¹, K.N. Nigussa^{2*}

¹Department of Physics, Haramaya University, P.O. Box 138, Dire Dawa, Ethiopia

²Department of Physics, Addis Ababa University, P.O. Box 1176, Addis Ababa, Ethiopia

Abstract

Proton transport property is studied by modelling the intermolecular pair correlation functions of the proton ion with the electrode and the electrolyte of a polymer electrolyte fuel cell (PEMFC) by using Materials-Studio and then applying molecular dynamics simulation. A stable structure of the novel electrode design is obtained using density functional theory. When the polymer electrolyte is assumed as anhydrous, the efficiency of the proton transport increases. Analysis of the proton coordination numbers shows that more protons are found in the region of oxygen than sulfur atoms of the Sulfonic acid Ether Ester Ketone (SEEK) electrolyte. The proton conductivity values are increased with including interaction effects from electrode compared to without. At a temperature of 333 K, these values of ion conductivity are $7.69 \times 10^5 \text{ S cm}^{-1}$ and $4.28 \times 10^5 \text{ S cm}^{-1}$, respectively, with and without. The network of the hydrogen bond is the path to transport of protons via the processes of hydrogen bond creating and breaking. The values of highest peaks in the radial distribution function ($g(r)$) calculations appear to fall in the hydrogen bond formation region. Thus, it looks that a combination of Pd₃Ag as an electrode and unhydrated SEEK as an electrolyte could make up for a cost effective components of new design PEMFC.

Keywords: Proton transport, PEMFC, SEEK, Hydrogen bond, Molecular dynamics simulations.

1. Introduction

Low temperature polymer electrolyte membrane fuel cells (PEMFC), also known as proton exchange membrane fuel cells, have stimulated interest in recent years as a feasible power source, particularly in automotive applications. PEM fuel cells generate electricity by combining hydrogen (or hydrogen-rich fuel) and oxygen (from the air), resulting in low pollution and high fuel economy [1]. The development of highly active and low-cost catalysts is a major challenge before proton exchange membrane fuel cells (PEMFCs) can find large-scale practical applications [2–9].

Platinum has been widely chosen for a catalytic role in PEMFC since a decades ago [10]. However, there is a need to find alternative material to replace Pt, since it has been used as a catalyst for fuel cells for a long time and might be in short supply in the future. One of the major barriers to commercialization of fuel cell engines is the electrodes' high cost, which is mostly due to the use of expensive platinum (Pt)-containing electro-catalysts. In addition, platinum-based catalysts can be poisoned by carbon monoxide (CO) and other pollutants [11]. Because of these characteristics, pursuing for alternative catalyst materials have gotten a lot of research attention. The oxygen reduction reaction (ORR) at the cathode in the PEM fuel cell is a rate-limiting phase, in which molecular oxygen is dissociated and mixed with protons and electrons supplied by the anode through the membrane and external circuit to form water as by-product.

A recent study by K.N. Nigussa [12] has investigated palladium as a possible candidate for replacement. This corresponds to $x = 0$, in the alloy composition. However, still because of the rare availability of Pd, consideration of further other alloys as a replacement candidate is of interest in this work. As a result, one of our primary motives is to investigate the properties of the Pd_{1-x}Ag_x ($x = 0.25 - 0.75$) alloy as components of fuel cell as electrode. This

*Corresponding author: kenate.nemera@aaau.edu.et (K.N. Nigussa)
Email address: sshinie21@gmail.com (S.S. Awulachew¹)

could also represent a study on a part of a grand alloy matrix $Pt_{1-x}Ag_xPd_{1-x}Ag_x$, making the fuel cell electrode, where investigating how certain region of the alloy dominated by $Pd_{1-x}Ag_x$ behaves is the central interest point of this work. Studying efficiency of candidate replacement catalysts goes through investigating interactions of molecules of fuel with components of the fuel cell as well as also transport of the molecules of fuel within the fuel cell. The ion dynamics in the electrolyte of the fuel cell is studied by Molecular Dynamics (MD). Thus, this activity is a conjugate study to our preceding study [13] on analysis of the property of Pd_3Ag (111) as a potential electrode component of a fuel cell. A simplified diagram of the PEM fuel cell operating principles is shown in Fig. 1.

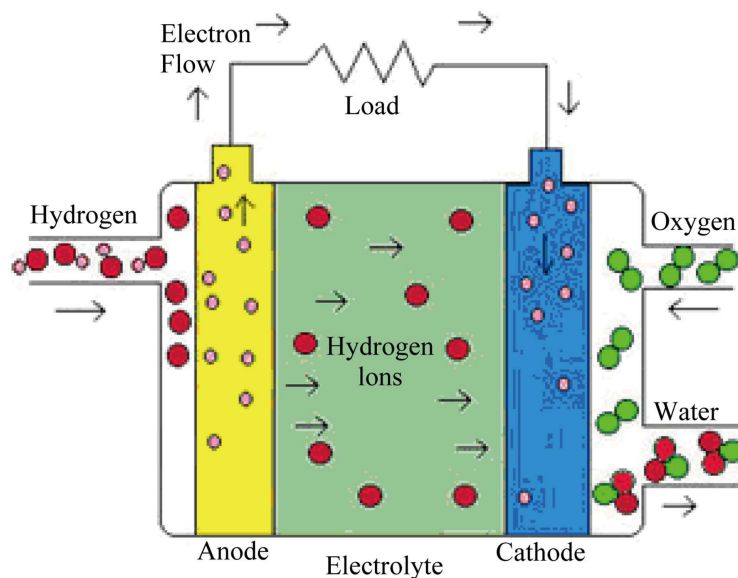


Figure 1: Simplified diagram of the PEM fuel cell operating process, taken from [11].

2. Computational Methods

2.1. Force Field

We assume a simplified model of PEMFCs. For this work, Sulfonic acid Ether Ester Ketone (SEEK) Polymer with chemical formula unit of $(C_{19}H_{14}O_{12}S_3)$ was used as electrolyte to investigate the proton conductivity, diffusion constant, radial distribution function, and coordination number, by developing a model as shown in Figs. 2 & 3. The Amorphous Cell (AC) for simulation was constructed with 400 protons (H^+), and 15 Sulfonated Ether Ester Ketone (SEEK) polymer chain. The AC was placed between layers of anode and cathode which are made of Pd_3Ag (111) alloy (see Fig. 3). At initial stages, the simulation cell was constructed by inserting the molecules randomly. The simulation system consists of H, C, S, O, Pd, and Ag atoms. The COMPASS force field is generated according to a literature [14], with a three-dimensional periodic boundary conditions being applied. A "smart" method was used to optimize the geometry of the cell. The final structures obtained from the geometry optimization process were heated to temperatures ranging from 200 K to 500 K. The annealing process was carried out five times. The dynamic simulation is done using the final structures created from the annealing procedure. The dynamic properties of these cells were studied using a 20 ps NVE production run following a 20 ps NVT equilibration. The Nose-Hoover approach was used to manage temperature during the simulation process. The time step was 1 fs and the setting of the temperature was (333 K, 383 K, 433 K). The cut-off radius of the non-bonded interactions was set to 12.5 Å. Ewald summation was employed for both van der Waals and Coulombic interactions [15, 16]. The total potential energy and temperature variations of the simulation systems during NVT equilibration and NVE production run are shown in Figs. 4-7.

As shown in the figures, the fluctuations were small and are in the normal range which can be seen to confirm occurrence of NVT equilibration. The temperature fluctuations and almost the unchanged energy may be caused by

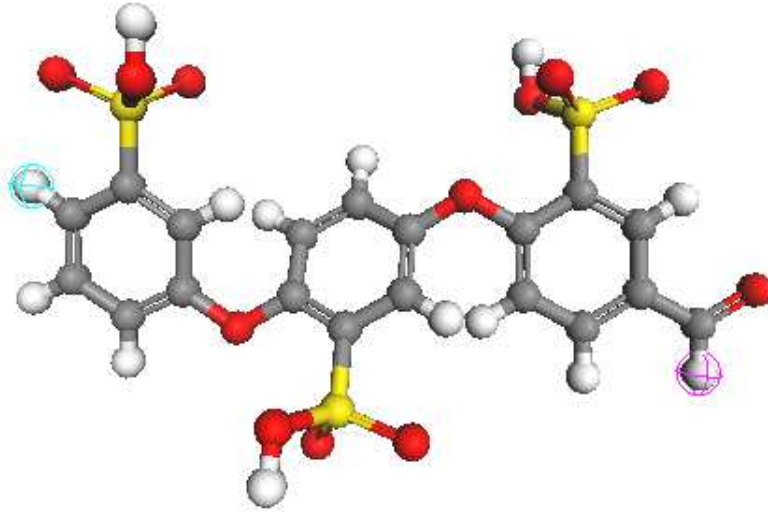


Figure 2: Sulfonic acid Ether Ester Ketone (SEEK). Color online. Colors: O-red, S-yellow, C-dark grey, and H-white.

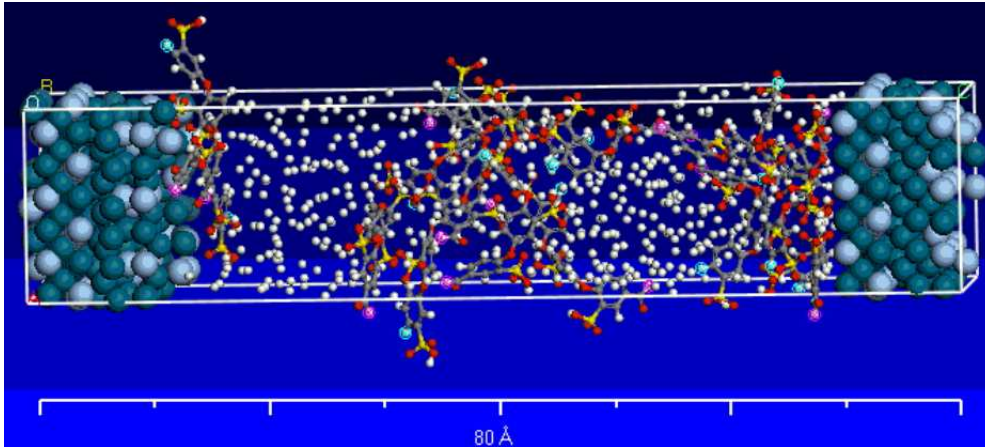


Figure 3: Fuel Cell Model for Hydrogen ion mobility with Pd₃Ag electrode and SEEK electrolyte. Color online. Colors: O-red, S-yellow, C-dark grey, H-white, Ag-cyan, and Pd-light grey.

the continuous transformation between kinetic energy and potential energy. For all cases, the volume of the simulation box is 23206.05 Å³. In the case of Pt and Pd electrodes, the Pd₃Ag (111) in Fig. 3 is replaced with Pt (111) and Pd (111), respectively.

2.2. Molecular Dynamics (MD) simulation

In the MD simulation, the mobile trajectory of proton can generate mean square displacement (MSD), and the average square of displacement, where a particle moves from time 0 to time t . The self-diffusion coefficient is directly related to the time of correlation of coordinates. The self-diffusion coefficients D is obtained from the slope of mean square displacement (MSD) as a function of time t according to the Einstein relation (see Eq. (1) and a literature [17]).

$$D = \frac{1}{6} \lim_{t \rightarrow \infty} \frac{dMSD(t)}{dt} \quad (1)$$

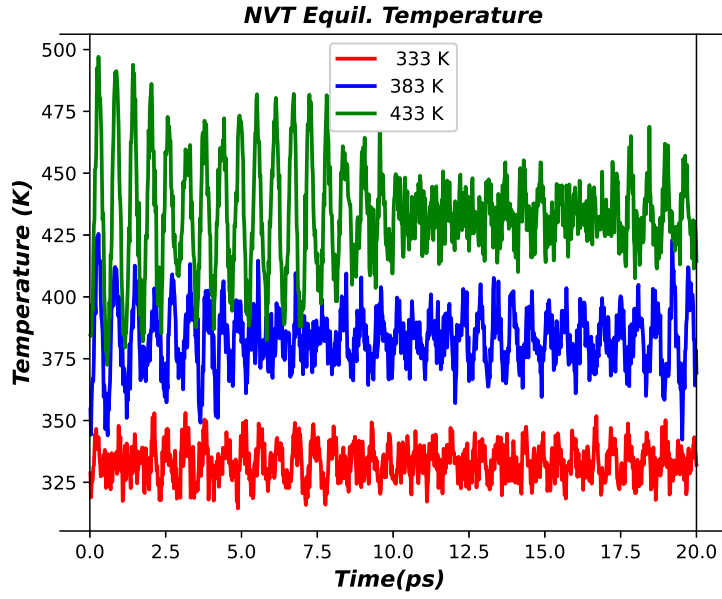


Figure 4: Temperature variation of the simulation system during NVT equilibration.

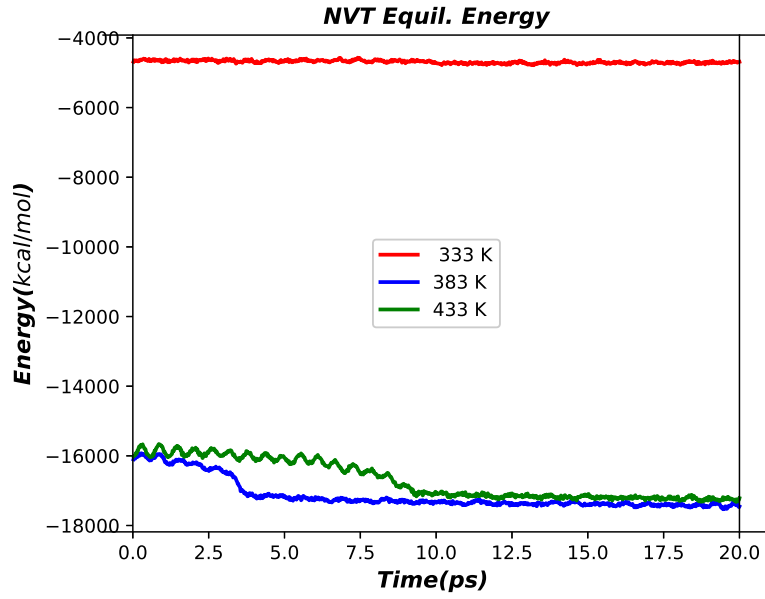


Figure 5: Total potential energy variation of the simulation system during NVT equilibration.

where MSD is defined as

$$MSD(t) = \left\langle \frac{1}{N} \sum_{i=1}^N |\mathbf{r}_i(t) - \mathbf{r}_i(0)|^2 \right\rangle \quad (2)$$

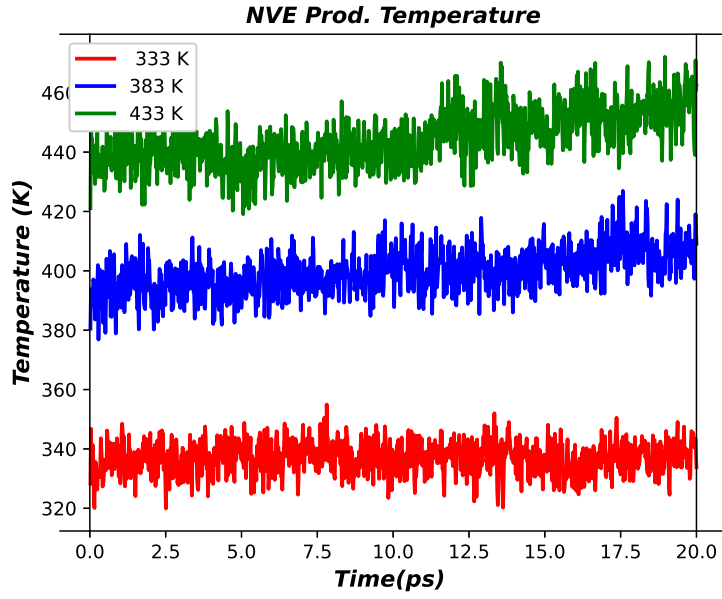


Figure 6: Temperature variation of the simulation system during NVE production run.

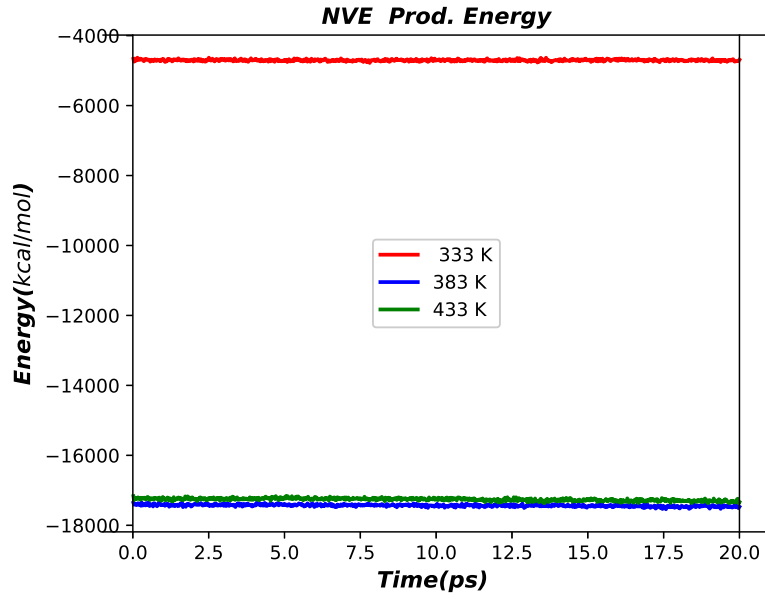


Figure 7: Total potential energy variation of the simulation system during NVE production run.

where $\mathbf{r}_i(t)$ is the position of the atom i at the time t , and the $\langle \dots \rangle$ denotes an average over all the time steps. N represents the number of diffusible particles. The proton conductivity (σ_{cond} , in units of Siemens per centimeter ($[S/cm]$))

is calculated using the diffusion coefficient of proton which is provided by Eq. (3),

$$\sigma_{cond} = \frac{Nz^2e^2}{Vk_B T} D_{\text{proton}} \quad (3)$$

in which N represents the number of protons, z is the charge on the proton (+1 in this study), e the elementary charge (1.6×10^{-19} C), D_{proton} is the diffusion coefficient of proton, V the volume of the simulation cell, k_B is the Boltzmann's constant (1.38×10^{-23} J/K), and T the absolute temperature.

Radial distribution function ($g(r)$) characterizes the local structure at short-range. It reflects the local structural arrangements around any given atom in a short distance and describes how distribution density varies as a function of distance.

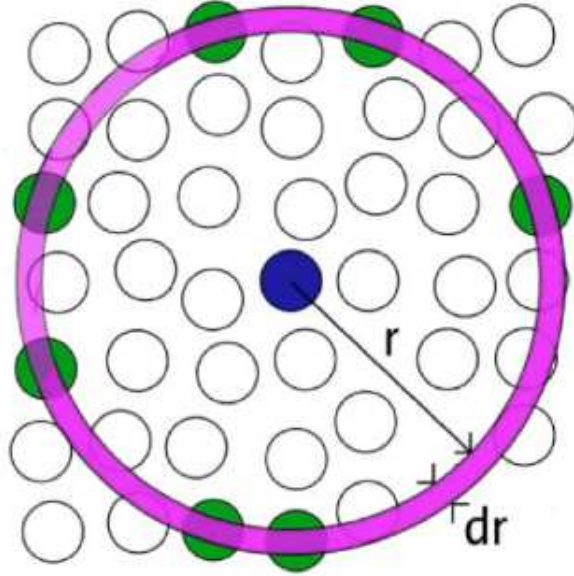


Figure 8: Space discretization for the evaluation of the radial distribution function, taken from [18].

For a homogeneous atomic system, the radial distribution function is shown in Fig. 8 (taken from [18]), where the blue particle is a reference particle at the origin O and green particles are those which are within the pink circular shell. If $\rho = \frac{N}{V}$ is the average number density of particles, then the local time-averaged density at a distance r from O is $\rho g(r)$. In other words, $g(r)$ involves determining how many particles are within a distance of r and $r + dr$ away from the blue particle at the origin. $g(r)$ is usually normalized as the ratio between the number of local particles and the average number of particles in the system. The normalized $g(r)$ also represents the probability of finding an atom in a shell dr at a distance r from a reference point atom. Thus, $g(r)$ can be used to calculate the number of atoms in the shell dr

$$dN(r) = \frac{N}{V} g(r) 4\pi r^2 dr \quad (4)$$

where $N(r)$ denotes the number of atoms as a function of location, N the total number of atoms, and V is the system's volume. When there are multiple chemical species, the partial radial distribution function $g_{\alpha\beta}(r)$ can be calculated by

$$g_{\alpha\beta}(r) = \frac{dN_{\alpha\beta}(r)}{4\pi r^2 dr \rho_\alpha} \quad (5)$$

where $\rho_\alpha = \frac{N_\alpha}{V}$ denotes the density of α species, and N_α denotes the total number of α species in the system.

3. Results and Discussion

3.1. Dynamics properties of protons

3.1.1. Pt as an Electrode

The dynamic properties of protons can be determined using the mean square displacement (MSD) of the protons during the simulation. As shown in Fig. 9, MSD of protons at 333 K is slightly increased in the presence of electrode

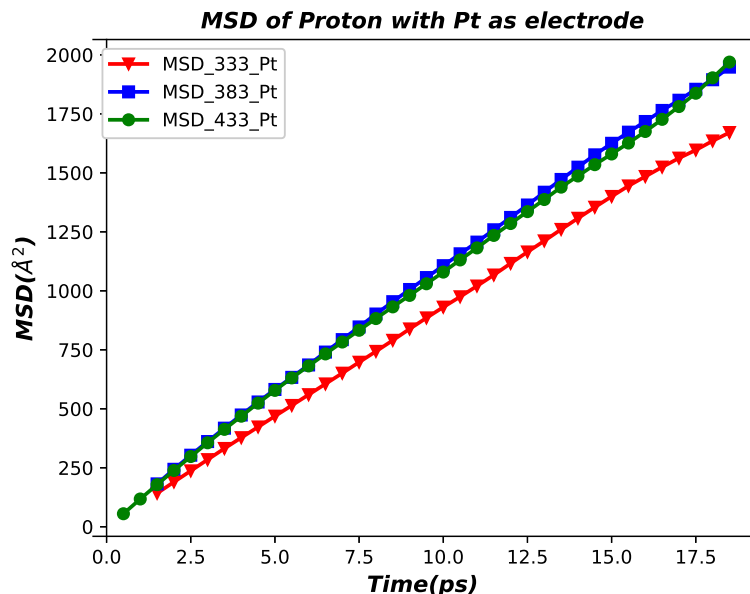


Figure 9: The mean square displacement (MSD) of protons. The simulations were carried out at 333 K, 383 K, and 433 K with Pt as electrode, over a period of 20 ps.

interaction. At 333 K, the self-diffusion coefficient of proton is $1.52 \times 10^{-3} \text{ cm}^2\text{s}^{-1}$, at 383 K, it is $1.73 \times 10^{-3} \text{ cm}^2\text{s}^{-1}$, and at 433 K, it is $1.72 \times 10^{-3} \text{ cm}^2\text{s}^{-1}$ as shown in Table 1.

It looks that the MSD value increases as temperature increases within the temperature range considered. The results were obtained using Eq. (2). The MSD plots at lower temperatures are shown in Fig. 10. The self-diffusion coefficient at temperatures of 200 K, 250 K, and 250 K, where interaction effects from electrode included are $1.18 \times 10^{-3} \text{ cm}^2\text{s}^{-1}$, $1.38 \times 10^{-3} \text{ cm}^2\text{s}^{-1}$ and $1.65 \times 10^{-3} \text{ cm}^2\text{s}^{-1}$, respectively, as shown in Table 1. The proton conductivity is calculated by using Eq. (3). The outcomes are $1.44 \times 10^6 \text{ S cm}^{-1}$, at 333 K, $1.41 \times 10^6 \text{ S cm}^{-1}$ at 383 K and $1.24 \times 10^6 \text{ S cm}^{-1}$ at 433 K as shown in Table 1. Furthermore, the computational results suggests that the conductivity decreases with temperature increases. The proton conductivity corresponding to temperatures of 200 K, 250 K, and 300 K, are $1.85 \times 10^6 \text{ S cm}^{-1}$, $1.73 \times 10^6 \text{ S cm}^{-1}$, and $1.72 \times 10^6 \text{ S cm}^{-1}$, respectively as shown in Table 1. Intermolecular pair correlation functions of O-H pair, S-H pair, at 333 K, 383 K and 433 K with Pt as an electrode are presented in Fig. 11.

The highest peaks and coordination number of O-H and S-H pair are presented in Table 1. All O-H pair highest peak distances falls well with in the range of a hydrogen bond. The intermolecular pair correlation functions of O-H pair, S-H pair, at 200 K, 250 K, and 300 K are shown in Fig. 12. The highest peaks of O-H pair intermolecular pair correlation functions occur at a positions of 2.35 Å, 2.35 Å, and 2.37 Å, for 200 K, 250 K, and 300 K, respectively. The coordination number of O-H pair are 41, 39, and 38, respectively, for 200 K, 250 K, and 300 K. The highest peaks of S-H pair intermolecular pair correlation functions are at a positions of 4.61 Å, 4.61 Å, and 4.23 Å, respectively, for 200 K, 250 K, and 300 K. The coordination number of S-H pair are 37, 36, and 35, respectively, for 200 K, 250 K, and, 300 K (as shown in Table 1). The fractional coordination numbers are results of a selected numerical integrator of the Eq. (4), and a corresponding nearest value integers can be used upon discussions.

Table 1: The maxima of the radial distribution functions in [\AA], conductivity in [S/cm] and coordination numbers of the O-H and S-H pair at different temperatures in [K]. The first two rows at 333 K (No eld.) for O-H and S-H is without electrode effect included in the interaction pair functions.

Electrode	Temperature	Correlation Pair	Highest Peak	Conductivity	Coordination Number	
Pt	333	O-H	2.35	1.44×10^6	38.24	
		S-H	4.33	1.44×10^6	34.24	
	383	O-H	2.35	1.41×10^6	38.12	
		S-H	4.59	1.41×10^6	34.12	
	433	O-H	2.41	1.24×10^6	36.47	
		S-H	4.59	1.24×10^6	32.49	
	200	O-H	2.35	1.85×10^6	40.60	
		S-H	4.61	1.85×10^6	37.28	
	250	O-H	2.35	1.73×10^6	39.14	
		S-H	4.61	1.73×10^6	35.83	
	300	O-H	2.37	1.72×10^6	38.54	
		S-H	4.23	1.72×10^6	35.00	
	Pd	333	O-H	2.37	1.41×10^6	38.62
			S-H	4.57	1.41×10^6	34.73
383		O-H	2.35	1.24×10^6	38.11	
		S-H	4.37	1.24×10^6	34.00	
433		O-H	2.37	1.31×10^6	38.32	
		S-H	4.57	1.31×10^6	33.80	
200		O-H	2.35	1.59×10^6	38.48	
		S-H	4.59	1.59×10^6	34.44	
250		O-H	2.33	2.01×10^6	41.28	
		S-H	4.57	2.01×10^6	36.99	
300		O-H	2.37	1.81×10^6	40.64	
		S-H	4.57	1.81×10^6	36.00	
Pd ₃ Ag		333 (No electrode)	O-H	2.37	4.28×10^5	40.72
			S-H	4.42	4.28×10^5	37.43
	383	O-H	2.35	7.69×10^5	34.48	
		S-H	4.37	7.69×10^5	30.53	
	383	O-H	2.37	7.56×10^5	37.17	
		S-H	4.77	7.56×10^5	33.82	
	433	O-H	2.37	7.46×10^5	35.27	
		S-H	4.23	7.46×10^5	31.01	
	200	O-H	2.33	9.37×10^5	35.10	
		S-H	4.45	9.37×10^5	31.10	
	250	O-H	2.33	9.09×10^5	35.98	
		S-H	4.41	9.09×10^5	31.93	
	300	O-H	2.35	7.33×10^5	33.91	
		S-H	4.63	7.33×10^5	29.94	

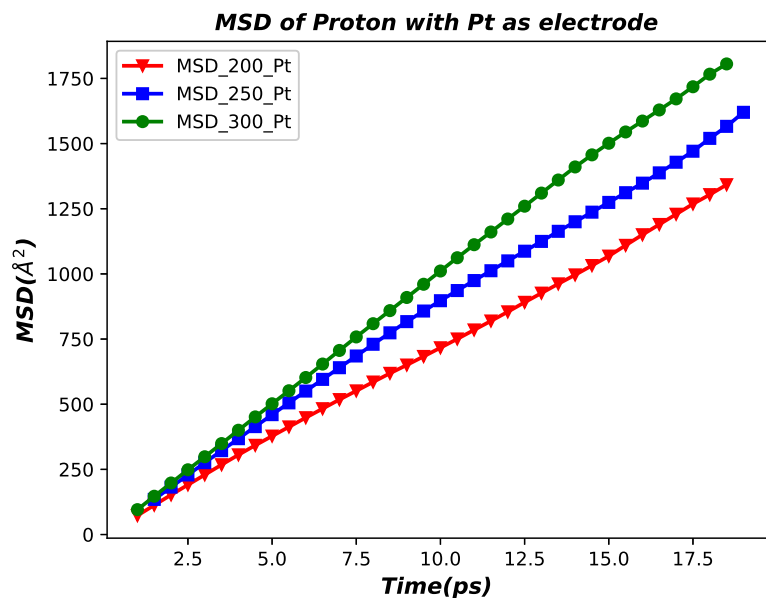


Figure 10: The mean square displacement (MSD) of protons. The simulations were carried out at 200 K, 250 K, and 300 K, with Pt electrode over a period of 20 ps. The electrode interaction effect is included.

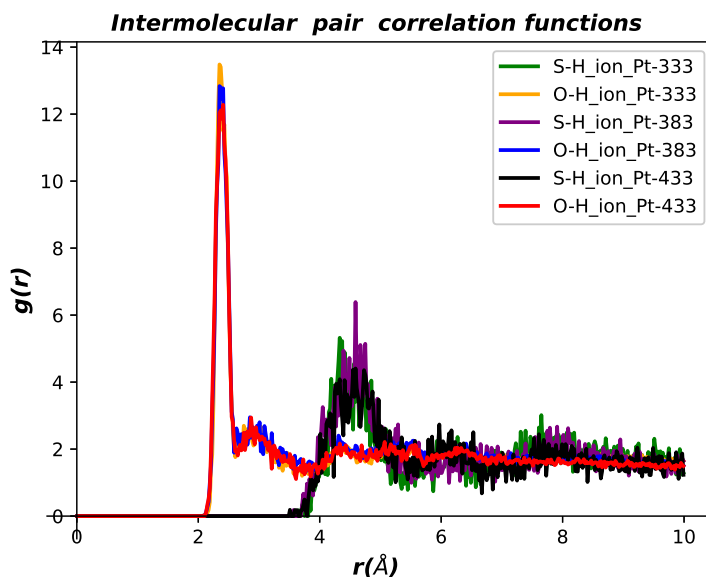


Figure 11: Intermolecular pair correlation functions of O-H and S-H at 333 K, 383 K, and 433 K with Pt electrode.

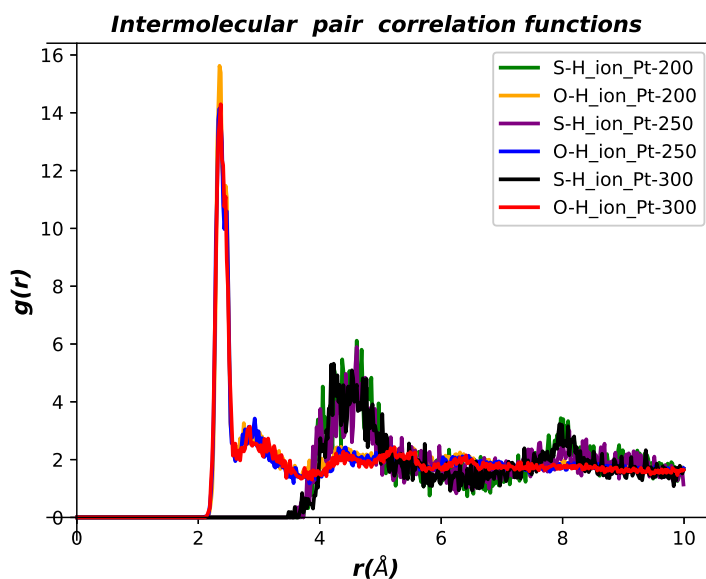


Figure 12: Intermolecular pair correlation functions of O-H and S-H at 200 K, 250 K and 300 K Pt electrode. Here the number of protons is 400.

All O-H pair highest peak distances fall well within the range of a hydrogen bond formation region. According to the values of highest peaks falls in hydrogen bond formation region, oxygen interacts with protons by creating hydrogen bonds, but sulfur interacts with protons at a greater distance than oxygen. The hydrogen bonding network can be used to transfer protons from anode to cathode.

3.1.2. Pd as an Electrode

As shown in Fig. 13, MSD of protons at 333 K is slightly increased in the presence of electrode interaction. At 333 K, the self-diffusion coefficient of proton is $1.53 \times 10^{-3} \text{ cm}^2\text{s}^{-1}$, at 383 K it is $1.55 \times 10^{-3} \text{ cm}^2\text{s}^{-1}$, and at 433 K it is $1.85 \times 10^{-3} \text{ cm}^2\text{s}^{-1}$ as shown in Table 1. It looks that the MSD value increases as temperature increases within the temperature range considered. The results were obtained using Eq. (2). The MSD plots at lower temperatures are shown in Fig. 14. The self-diffusion coefficient at temperatures of 200 K, 250 K, and 250 K, where interaction effects from electrode are included are $1.04 \times 10^{-3} \text{ cm}^2\text{s}^{-1}$, $1.64 \times 10^{-3} \text{ cm}^2\text{s}^{-1}$, and $1.77 \times 10^{-3} \text{ cm}^2\text{s}^{-1}$, respectively as shown in Table 1.

The proton conductivity is calculated by using Eq. (3). The outcomes are $1.41 \times 10^6 \text{ S cm}^{-1}$ at 333 K, $1.24 \times 10^6 \text{ S cm}^{-1}$ at 383 K and $1.31 \times 10^6 \text{ S cm}^{-1}$ at 433 K as shown in Table 1. Furthermore, the computational results suggest that the conductivity decreases with temperature increases. The proton conductivity corresponding to temperatures of 200 K, 250 K, and 300 K, are $1.59 \times 10^6 \text{ S cm}^{-1}$, $2.01 \times 10^6 \text{ S cm}^{-1}$, and $1.81 \times 10^6 \text{ S cm}^{-1}$, respectively as shown in Table 1. Intermolecular pair correlation functions of O-H pair, S-H pair, at 333 K, 383 K and 433 K with Pd as an electrode are presented in Fig. 15.

The highest peaks and coordination number of O-H and S-H pair are presented in Table 1. All O-H pair highest peak distances falls well within the range of a hydrogen bond.

The intermolecular pair correlation functions of O-H pair, S-H pair, at 200 K, 250 K, and 300 K are shown in Fig. 16. The highest peaks of O-H pair intermolecular pair correlation functions occur at a positions of 2.35 Å, 2.35 Å, and 2.37 Å, for 200 K, 250 K, and 300 K, respectively. The coordination number of O-H pair are 41, 39, and 38, respectively, for 200 K, 250 K, and 300 K. The highest peaks of S-H pair intermolecular pair correlation functions are at a positions of 4.61 Å, 4.61 Å, and 4.23 Å, respectively, for 200 K, 250 K, and 300 K. The coordination number of S-H pair are 37, 36, and 35, respectively, for 200 K, 250 K, and, 300 K (as shown in Table 1). The fractional coordination numbers are results of a selected numerical integrator of the Eq. (4), and a corresponding nearest value

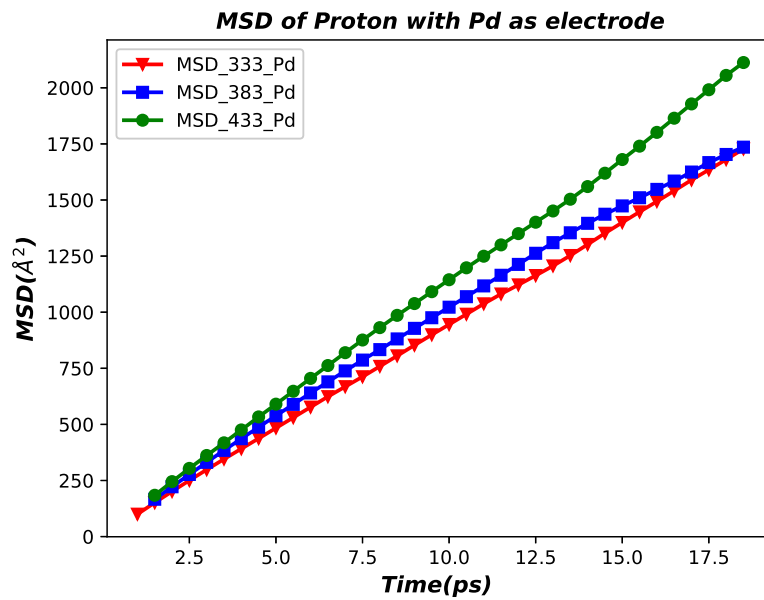


Figure 13: The mean square displacement (MSD) of protons. The simulations were carried out at 333 K, 383 K and 433 K with Pd as electrode, over a period of 20 ps.

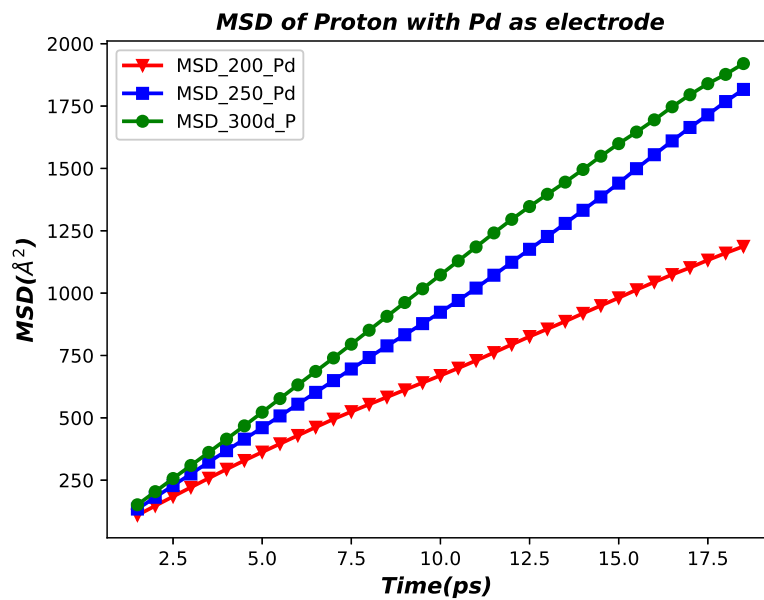


Figure 14: The mean square displacement (MSD) of protons. The simulations were carried out at 200 K, 250 K, and 300 K, with Pd electrode over a period of 20 ps. The electrode interaction effect is included.

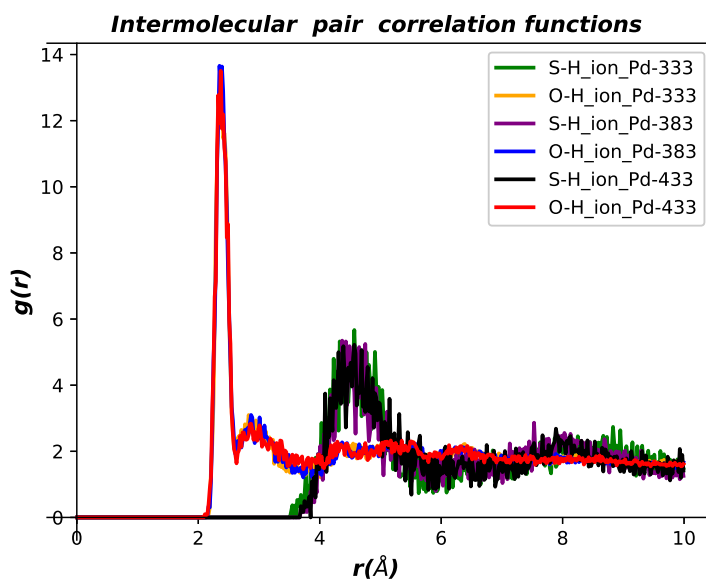


Figure 15: Intermolecular pair correlation functions of O-H and S-H at 333 K, 383 K, and 433 K with Pd electrode.

integers can be used upon discussions.

All O-H pair highest peak distances fall well within the range of a hydrogen bond formation region. According

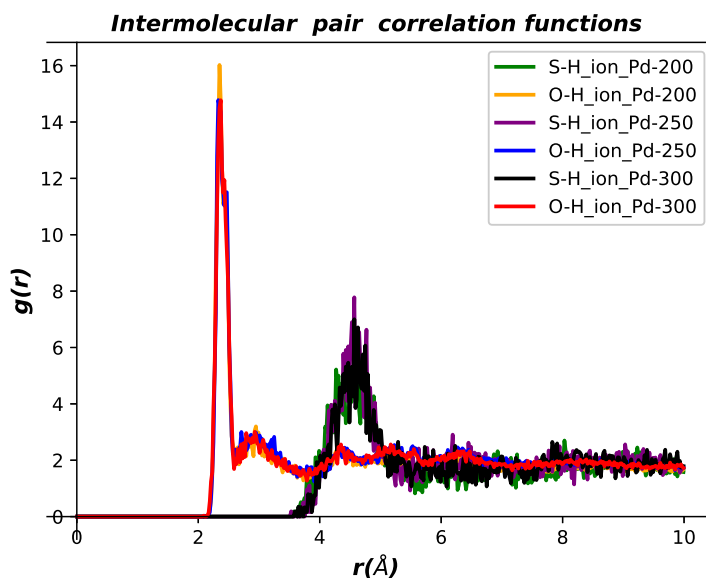


Figure 16: Intermolecular pair correlation functions of O-H and S-H at 200 K, 250 K and 300 K with Pd electrode. Here the number of protons is 400.

to the values of highest peaks falls in hydrogen bond formation region, oxygen interacts with protons by creating hydrogen bonds, but sulfur interacts with protons at a greater distance than oxygen.

3.1.3. Pd₃Ag as an Electrode

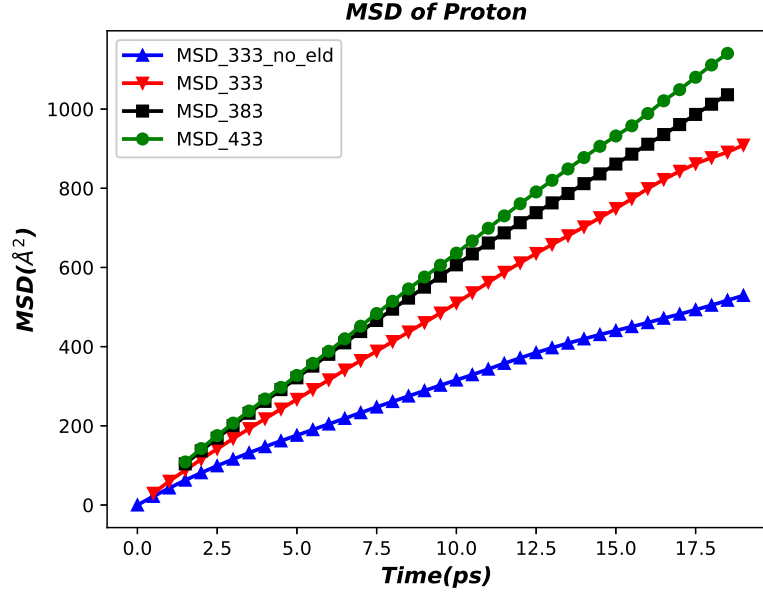


Figure 17: The mean square displacement (MSD) of protons. The simulations were carried out at 333 K with and without electrode, at 383 K and 433 K with Pd₃Ag electrode, over a period of 20 ps.

As shown in Fig. 17, MSD of protons at 333 K is increased in the presence of electrode interaction than without electrode. So, thus, at 383 K, and 433 K, the simulations are done by including interaction effects from electrode. At 333 K with electrode, the self-diffusion coefficient of proton is $8.01 \times 10^{-4} \text{ cm}^2\text{s}^{-1}$, while without electrode it is $4.46 \times 10^{-4} \text{ cm}^2\text{s}^{-1}$, at 383 K with electrode it is $9.06 \times 10^{-4} \text{ cm}^2\text{s}^{-1}$, and at 433 K with electrode it is $1.01 \times 10^{-3} \text{ cm}^2\text{s}^{-1}$ as shown in Table 1. It looks that the MSD value increases as temperature increases within the temperature range considered. The results were obtained using Eq. (2). The MSD plots at lower temperatures as shown in Fig. 18. The self-diffusion coefficient at temperatures of 200 K, 250 K, and 250 K, where interaction effects from electrode are included are $5.86 \times 10^{-4} \text{ cm}^2\text{s}^{-1}$, $7.11 \times 10^{-4} \text{ cm}^2\text{s}^{-1}$ and $6.88 \times 10^{-4} \text{ cm}^2\text{s}^{-1}$, respectively as shown in Table 1.

The proton conductivity is calculated by using Eq. (3). The outcomes are $4.28 \times 10^5 \text{ S cm}^{-1}$, and $7.69 \times 10^5 \text{ S cm}^{-1}$, respectively, without and with electrode, at 333 K. At temperatures of 383 K and 433 K and in the presence of interaction effect from electrode, the values of conductivity are $7.56 \times 10^5 \text{ S cm}^{-1}$, and $7.46 \times 10^5 \text{ S cm}^{-1}$, respectively as shown in Table 1. Furthermore, the computational results suggests that the conductivity decreases as temperature increases. The proton conductivity corresponding to temperatures of 200 K, 250 K, and 300 K, are $9.37 \times 10^5 \text{ S cm}^{-1}$, $9.09 \times 10^5 \text{ S cm}^{-1}$, and $7.33 \times 10^5 \text{ S cm}^{-1}$, respectively as shown in Table 1. Intermolecular pair correlation functions of O-H pair, S-H pair, at different temperature without and with electrode are illustrated in Fig. 19.

The highest peaks and coordination number of O-H and S-H pair by adding water to the system without electrode are calculated with values 2.37 Å and 36.49 for O-H pair, and 4.41 Å and 31.63 for S-H. Details are presented in Table 1. From the computational results, the value for dehydrated system is higher than the hydrated. The MSD for dehydrated system is greater than the hydrated system, with a value of $3.49 \times 10^{-4} \text{ cm}^2\text{s}^{-1}$ at 333 K. All O-H pair highest peak distances falls well within the range of a hydrogen bond.

The intermolecular pair correlation functions of O-H pair, S-H pair, at 200 K, 250 K, and 300 K are shown in Fig. 20. The highest peaks of O-H pair intermolecular pair correlation functions occur at a positions of 2.33 Å, 2.33 Å, and 2.35 Å, for 200 K, 250 K, and 300 K, respectively. The coordination number of O-H pair are 35, 36, and 34, respectively, for 200 K, 250 K, and 300 K. The highest peaks of S-H pair intermolecular pair correlation functions are at a positions of 4.45 Å, 4.41 Å, and 4.63 Å, respectively, for 200 K, 250 K, and 300 K. The coordination number of S-H pair are 31, 32, and 30, respectively, for 200 K, 250 K, and, 300 K (as shown in Table 1). The fractional

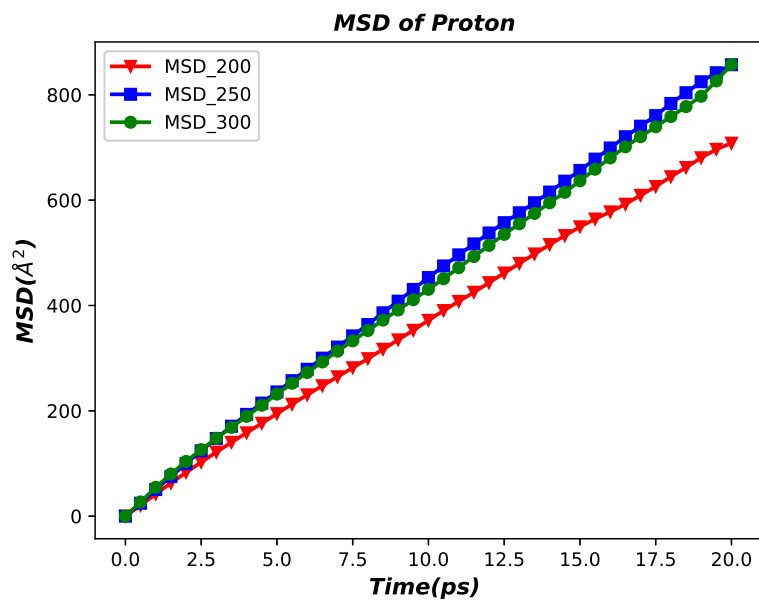


Figure 18: The mean square displacement (MSD) of protons. The simulations were carried out at 200 K, 250 K, and 300 K, with Pd₃Ag electrode, over a period of 20 ps. The electrode interaction effect is included.

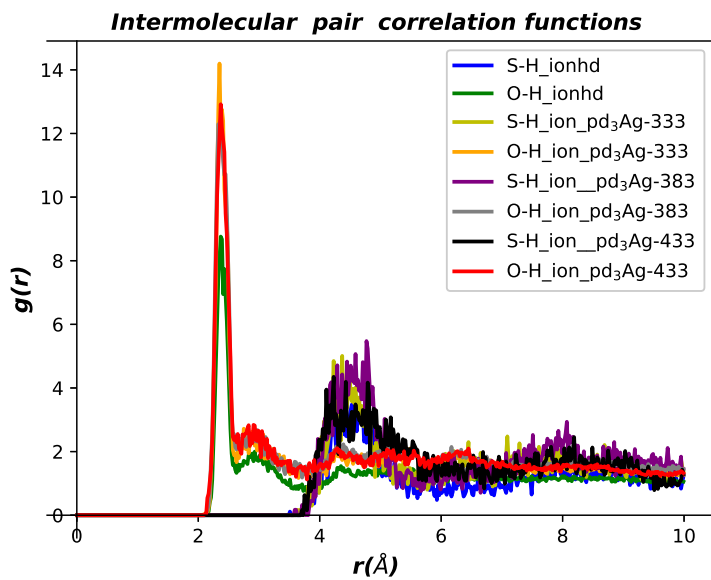


Figure 19: Intermolecular pair correlation functions of O-H and S-H at 333 K with and without electrode, at 383 K and 433 K with Pd₃Ag electrode.

coordination numbers are results of a selected numerical integrator of the Eq. (4), and a corresponding nearest value integers can be used upon discussions.

All O-H pair highest peak distances fall well within the range of a hydrogen bond formation region. The coordi-

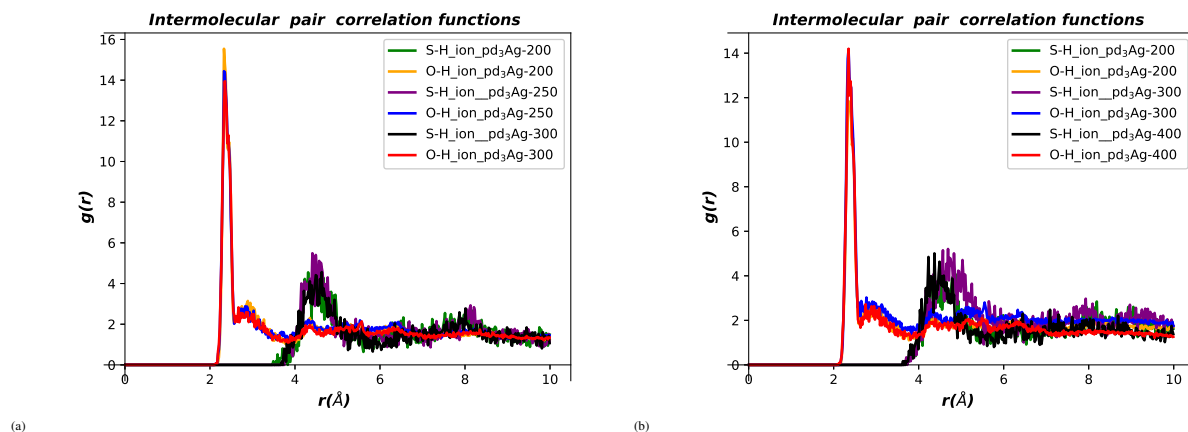


Figure 20: a) Intermolecular pair correlation functions of O-H and S-H at 200 K, 250 K and 300 K with Pd_3Ag electrode. Here the number of protons is 400 (left side). b) Number of protons being 200, 300, and 400 at a temperature of 333 K (right side).

nation numbers and position of highest peak of O-H pair and S-H pair for different temperatures are given in Table 1. According to the values of highest peaks falls in hydrogen bond formation region, oxygen interacts with protons by creating hydrogen bonds, but sulfur interacts with protons at a greater distance than oxygen. The hydrogen bonding network can be used to transfer protons from anode to cathode.

4. Conclusion

The molecular dynamics simulation results suggest that the conductivity of proton ions in the fuel cell decreases as temperature increases. The intermolecular pair correlation functions and coordination numbers show that the sulfonic acid group has significant interactions and hydrogen bonding. The proton mobility is aided by hydrogen bonds forming and breaking since the highest peaks of O-H are in the range of hydrogen bond formation. Proton transport can be facilitated by a network of hydrogen bonds. When Pt is included in the PEMFCs model, proton conductivity is relatively higher compared to proton conductivity when Pd or Pd_3Ag is used as an electrode. When Pt/ Pd / Pd_3Ag is included in the PEMFCs interaction model, proton conductivity is improved compared to proton conductivity without electrode contribution. The conductivity values of proton ions with the SEEK electrolyte and Pt electrode is in the range $[1.44 \times 10^6, 1.85 \times 10^6] \text{ S/cm}$, when the temperature increases in the range [200, 433] K. The conductivity values of proton ions with the SEEK electrolyte and Pd electrode is in the range $[1.31 \times 10^6, 1.81 \times 10^6] \text{ S/cm}$, when the temperature increases in the range [200, 433] K. The conductivity values of proton ions with the SEEK electrolyte and Pd_3Ag electrode is in the range $[7.69 \times 10^5, 7.46 \times 10^5] \text{ S/cm}$, when the temperature increases in the range [200, 433] K. The ion transport properties predicted with all potential electrodes is good enough. Furthermore, the ion conductivity for Pd_3Ag electrode of PEMFC is reduced only by a factor of half compared to the ion conductivity with either of the Pt electrode PEMFC or Pd electrode PEMFC. Thus, Pd_3Ag can function smoothly in replacing the Pt electrode PEMFC. Furthermore, dehydrated SEEK electrolyte performs relatively better than hydrated SEEK electrolyte.

Disclosure statement

The authors declare that there is no conflict of interest.

Acknowledgments

We are grateful to the Ministry of Education of Ethiopia for financial support. The authors also acknowledge the Department of Physics at Addis Ababa University. The office of VPRTT of Addis Ababa university is also warmly appreciated for supporting this research under a grant number AR/053/2021.

References

References

- [1] W. Vielstich, H. A. Gasteiger, H. Yokokawa, *Handbook of fuel cells: advances in electrocatalysis, materials, diagnostics and durability*, Vol. 5, John Wiley & Sons, 2009.
URL <https://doi.org/10.1002/cphc.200490023>
- [2] A. Wieckowski, E. R. Savinova, C. G. Vayenas, *Catalysis and electrocatalysis at nanoparticle surfaces*, CRC Press, 2003.
URL <https://doi.org/10.1201/9780203912713>
- [3] P. Weber, D. J. Weber, M. Janssen, M. Werheid, M. Oezaslan, *Carbon supported Pt-Co Alloy Nanoparticles as HOR and ORR catalyst for PEM fuel cells*, in: ECS Meeting Abstracts, no. 44, IOP Publishing, 2018, p. 1483.
URL <https://doi.org/10.1149/ma2018-02/44/1483>
- [4] E. Antolini, *Formation of carbon-supported PtM alloys for low temperature fuel cells: a review*, *Materials chemistry and physics* 78 (3) (2003) 563–573.
URL [https://doi.org/10.1016/S0254-0584\(02\)00389-9](https://doi.org/10.1016/S0254-0584(02)00389-9)
- [5] Y. Shao, G. Yin, Y. Gao, *Understanding and approaches for the durability issues of Pt-based catalysts for PEM fuel cell*, *Journal of Power Sources* 171 (2) (2007) 558–566.
URL <https://doi.org/10.1016/j.jpowsour.2007.07.004>
- [6] X. Yu, S. Ye, *Recent advances in activity and durability enhancement of Pt/C catalytic cathode in PEMFC: Part I. Physico-chemical and electronic interaction between Pt and carbon*, *Journal of power sources* 172 (1) (2007) 133–144.
URL <https://doi.org/10.1016/j.jpowsour.2007.07.049>
- [7] J. Chen, B. Lim, E. P. Lee, Y. Xia, *Shape-controlled synthesis of platinum nanocrystals for catalytic and electrocatalytic applications*, *Nano Today* 4 (1) (2009) 81–95.
URL <https://doi.org/10.1016/j.nantod.2008.09.002>
- [8] Z. Peng, H. Yang, *Designer platinum nanoparticles: control of shape, composition in alloy, nanostructure and electrocatalytic property*, *Nano today* 4 (2) (2009) 143–164.
URL <https://doi.org/10.1016/j.nantod.2008.10.010>
- [9] Z. Liu, G. S. Jackson, B. W. Eichhorn, *Tuning the CO-tolerance of Pt-Fe bimetallic nanoparticle electrocatalysts through architectural control*, *Energy & Environmental Science* 4 (5) (2011) 1900–1903.
URL <https://doi.org/10.1039/C1EE01125A>
- [10] L. Hunt, F. Lever, *Availability of the Platinum Metals*, *Platinum Metals Rev.* 13 (4) (1971) 126.
URL <https://doi.org/10.1021/ba-1971-0098.ch005>
- [11] M. Shao, T. Huang, P. Liu, J. Zhang, K. Sasaki, M. Vukmirovic, R. Adzic, *Palladium monolayer and palladium alloy electrocatalysts for oxygen reduction*, *Langmuir* 22 (25) (2006) 10409–10415.
URL <https://pubs.acs.org/doi/10.1021/la0610553>
- [12] K. N. Nigussa, *A study of properties of palladium metal as a component of fuel cells*, *Materials Research Express* 6 (10) (2019) 105540.
URL <https://doi.org/10.1088/2053-1591/ab3fd4>
- [13] S. S. Awulachew, K. N. Nigussa, *First principles and Monte Carlo studies of adsorption and desorption properties from Pd_{1-x}Ag_x surface alloy (2022)*. [arXiv:2204.02812](https://arxiv.org/abs/2204.02812).
- [14] H. Sun, *COMPASS: an ab initio force-field optimized for condensed-phase applications overview with details on alkane and benzene compounds*, *The Journal of Physical Chemistry B* 102 (38) (1998) 7338–7364.
URL <https://doi.org/10.1021/jp980939v>
- [15] T. M. Nymand, P. Linse, *Ewald summation and reaction field methods for potentials with atomic charges, dipoles, and polarizabilities*, *The Journal of Chemical Physics* 112 (14) (2000) 6152–6160.
URL <https://doi.org/10.1063/1.481216>
- [16] A. Ibrahim, O. Hossain, J. Chaggar, R. Steinberger-Wilckens, A. El-Kharouf, *Go-nafion composite membrane development for enabling intermediate temperature PEM fuel cells*, *International Journal of Hydrogen Energy* 45 (8) (2020) 5526–5534.
URL <https://doi.org/10.1016/j.ijhydene.2019.05.210>
- [17] P. Cummings, B. Wang, D. Evans, K. Fraser, *Nonequilibrium molecular dynamics calculation of self-diffusion in a non-Newtonian fluid subject to a Couette strain*, *The Journal of chemical physics* 94 (3) (1991) 2149–2158.
URL <https://doi.org/10.1063/1.459886>
- [18] M. P. Allen, D. J. Tildesley, *How to analyse the results*, in: *Computer Simulation of Liquids*, Oxford University Press, 1987.